Luminescence properties of Ce^{3+} and Tb^{3+} co-doped SiO_xN_y thin films: Prospects for color tunability in silicon-based hosts

J. M. Ramírez[1,a),b)], A. Ruiz-Caridad[1], J. Wojcik[2], A. M. Gutierrez[3], S. Estradé[1], F. Peiró[1], P. Sanchís[3], P. Mascher[2] and B. Garrido[1]

[1]MIND-IN2UB, Departament d'Electrònica, Universitat de Barcelona, Martí i Franquès 1, 08028, Spain

[2]Department of Engineering Physics and Centre for Emerging Device Technologies, McMaster University,1280 Main St. W, Hamilton, Ontario L8S4L7, Canada

[3]Nanophotonics Technology Center, Universitat Politècnica València, 46022 Spain

In this work, the role of the nitrogen content, the annealing temperature and the sample morphology on the luminescence properties of Ce^{3+} and Tb^{3+} co-doped SiO_xN_y thin films has been investigated. An increasing nitrogen atomic percentage has been incorporated in the host matrix by gradually replacing oxygen by nitrogen during fabrication while maintaining the Si content unaltered, obtaining a sequential variation in the film composition from nearly stoichiometric SiO_2 to SiO_xN_y. The study of rare earth doped single layers has allowed us to identify the parameters that yield an optimum optical performance from Ce^{3+} and Tb^{3+} ions. Ce^{3+} ions proved to be highly sensitive to the annealing temperature and the nitrogen content, showing strong PL emission for relatively low nitrogen contents (from 0 to 20 %) and moderate annealing temperatures (800-1000 °C) or under high temperature annealing (1180 °C). Tb^{3+} ions, on the other hand, displayed a mild dependence on those film parameters. Rare earth co-doping has also been investigated by comparing the luminescence properties of three different approaches: (i) a Ce^{3+}- and Tb^{3+} co-doped SiO_xN_y single layer, (ii) a bilayer composed of two SiO_xN_y single layers doped with either Ce^{3+} or Tb^{3+} ions, and (iii) a multilayer composed of a series of either Tb^{3+} or Ce^{3+}-doped SiO_xN_y thin films with interleaved SiO_2 spacers. Bright green emission and efficient energy transfer from either Ce^{3+} ions or Ce silicates to Tb^{3+} ions has been observed in the co-doped single layer as a consequence of the strong ion-ion interaction. On the other hand, independent luminescence from Ce^{3+} and Tb^{3+} ions has been observed in the Ce^{3+} and Tb^{3+} co-doped bilayer and multilayer, providing a good scenario to develop light emitting devices with wide color tunability by varying the number of deposited films that contain each rare earth dopant. Moreover, the optoelectronic properties of Ce^{3+}- and/or Tb^{3+}-doped thin films have been studied by depositing transparent conductive electrodes over selected samples. An electroluminescence signal according to the rare earth transitions is obtained in all cases, validating the excitation of Ce^{3+} and Tb^{3+} ions upon electron injection. Also, the main charge transport of injected electrons has been evaluated and correlated with the layer stoichiometry. Finally, a simple

[a)] Now at Institut d'Electronique Fondamentale, Univ. Paris-Sud, CNRS, Univ. Paris-Saclay, UMR 8622, Bât. 220, 91405 Orsay Cedex, France

[b)] Corresponding author: joan-manel.ramirez@u-psud.fr

reliability test has allowed disclosing the origin of the early breakdown of test devices, attributed to the excessive joule heating at filament currents that occur around a region close to the polarization point.

I. INTRODUCTION

One of the key milestones of Silicon Photonics is the development of an efficient, sustainable and cost-effective electrically driven light source fully compatible with CMOS technology.[1,2,3] This new device is expected to provide solutions to most of the inherent bottlenecks of the current microelectronics industry, as it would reduce the overheating and latency times that are often attributed to the large number of interconnects in nowadays microelectronic chips, while enabling a high-speed data on-chip communication network with much wider operation bandwidths.[4] Aside from telecom, the implementation of low-cost integrable silicon-based light sources would also benefit other growing niche markets such as the microdisplay industry or the sensing technologies.[5,6,7,8] Up to now, several approaches have been employed to develop Si-based light sources. Among them, the most remarkable are the ones that introduce intraband dislocation loops to enhance the radiative recombination of excitons at specific trapping sites in p-n junctions or the nanostructuring of Si in the form of silicon nanocrystals (Si-ncs) to benefit from their superior optical properties compared to bulk silicon.[9,10] However, the fast aging of devices, the limited color tunability of the emission and the rather low room temperature efficiency provided by these systems motivated the search for alternative solutions to fulfill the requirements on demand. Also worth noting are the hybrid approaches that combine either direct bandgap materials (III-V or II-VI), organic or polymeric compounds bonded (or deposited) over Si substrates.[11] So far, this method has become the most successful in terms of device performance, since outstanding optoelectronic characteristics from light emitting diodes (LEDs) or hybrid silicon lasers have already been demonstrated.[12-15] Nevertheless, in spite of the exceptional properties displayed in this case, the success of the above mentioned technology is compromised by several critical alignment steps and more expensive raw materials that increase the final cost of devices. Thus, a truly monolithic electrically driven light source in which the optical and electrical functionalities are designed and fabricated together using a single and standardized technological process is desired for the medium to long term. In the search for that goal, another popular strategy that has been implemented by several authors consists of taking advantage of the narrow emission lines provided by radiative de-excitations of inner rare earth (RE) transitions when ions are located in suitable host environments that yield the appropriate oxidation state.[16-22] In that regard, silicon oxides (SiO_2) and silicon-rich oxides (SiO_x) thin films have proved to be good hosts for a wide variety of RE ions, since intense electroluminescence (EL) has been demonstrated when embedded in metal-oxide-semiconductor (MOS) devices.[5] Among them, Er^{3+}-doped SiO_2 (SiO_x) thin films are of particular interest since they show an

intense EL emission at 1.55 μm that is suitable for the development of integrated light sources operating at telecom wavelengths.[2327] On the other hand, Ce^{3+}, Tb^{3+} and Eu^{3+}-doped SiO_2 (SiO_x) thin films showed encouraging properties to develop integrated red-green-blue micro-displays.[28-31] Despite this interesting scenario, RE-doped oxides also present important drawbacks that need to be overcome, such as the high voltage operation for the EL threshold, the formation of non-emitting RE clusters inside the SiO_2 or the progressive film degradation as a consequence of the continuous hot carrier injection under electrical pumping.[23-25] Such detrimental performance is mostly caused by the large bandgap of SiO_2, which is around ~ 9 eV. Therefore, silicon nitride (Si_3N_4) has often been postulated as a promising host material to replace SiO_2, as it has much lower bandgap (~ 4 eV), is silicon compatible and provides a suitable environment for RE ions.[26-28] Unfortunately, with direct impact excitation of hot electrons being the main excitation mechanism of RE ions under electrical pumping, Si_3N_4 also presents lower RE excitation efficiency as the number of injected hot carriers is much lower than in SiO_2.[29] In view of this scenario, the exploration of new CMOS compatible materials to be used as hosts for RE ions in Si-based light sources is still ongoing. In that regard, one of the promising compounds is SiO_xN_y. This material, if grown with the appropriate parameters, may retain the advantages of SiO_2 and Si_3N_4 while providing additional benefits such as low mechanical stress or good resistance to oxidation.[30-35] We shall note that although previous works have already suggested this matrix as suitable for the development of RE-doped Si-based light sources, the role of several key fabrication parameters on their optical properties has not yet been studied in detail. Similarly, the luminescence properties of rare earth co-doped thin films, in which the ion-ion interaction is controlled at will to yield different spectral patterns has not yet been explored. Therefore, this work focuses on the study of the optical properties of Ce^{3+}- and Tb^{3+}-doped SiO_xN_y thin films for the development of widely tunable Si-based light sources. Firstly, thin films with a single RE dopant (either Ce^{3+} or Tb^{3+}) were fabricated and characterized to disclose the best annealing temperature and the most favorable nitrogen atomic percentage that yields an outstanding performance. Based on these results, the co-doping approach was also investigated in several samples containing different morphologies: (i) a single layer with Ce^{3+} and Tb^{3+} ions randomly distributed, (ii) a bilayer composed of a Ce^{3+}-doped and a Tb^{3+}-doped single layer (different RE species are deposited sequentially) and (iii) a multilayer design in which Ce^{3+}-doped and Tb^{3+}-doped single layers are physically separated by thin SiO_2 spacers to prevent mixing of RE ions during annealing. Intense and tunable luminescence from cobalt blue to emerald green is demonstrated under daylight conditions. Finally, a first inspection of the optoelectronic properties of RE-doped thin films was performed after deposition of transparent conductive electrodes over selected samples. Several charge transport mechanisms were identified and correlated with film stoichiometry, EL and layer degradation.

II. MATERIALS AND METHODS

Thin films were deposited by electron cyclotron plasma enhanced chemical vapour deposition (ECR-PECVD) on a highly n-type doped double side polished Si wafer (<100> oriented) using three different precursor gases diluted in Ar (SiH_4 at 30 %,

O_2 at 10 % and N_2 at 10 %). Departing from a nearly stoichiometric SiO_2 film using only SiH_4/Ar and O_2/Ar lines (operating at 2.5 and 25 sccm, respectively), the composition was then gradually varied by increasing the N_2/Ar gas flow rate from 0 to 25 sccm in steps of 5 sccm while evenly decreasing the O_2/Ar gas flow rate by the same amount. A gradual replacement of oxygen by nitrogen was expected in the matrix. Base and operating pressure values of $4.3 \cdot 10^{-4}$ and $3 \cdot 10^{-3}$ Torr were measured, respectively. An average deposition rate of ~ 0.25 Å$\cdot s^{-1}$ was established, yielding a final nominal thickness of 90 nm for all samples (1 h of deposition). Ce^{3+} and Tb^{3+} ions were incorporated by means of an in-situ doping system composed of a heated RE diffusion cell loaded with a β-diketonate organic compound ($Tb[tmhd]_3$ for Tb incorporation and $Ce[tmhd]_4$ for Ce doping) connected to a couple of RE shower head towers that are located in front of the Si substrate. Finally, deposited samples underwent an annealing treatment for 1 h in an inert N_2 ambient at different temperatures ranging from 500 °C up to 1180 °C, in steps of 100 °C.[36] Such fabrication procedure, with only the Si precursor gas containing a potential H_2 source (in the form of SiH_4) combined with the moderately high annealing temperatures and the hydrogen-free annealing environment (N_2) used is expected to minimize the undesired Si-OH, Si-H and N-H bonds that are commonly identified in samples fabricated by plasma enhanced techniques.[37,38] Further details of sample fabrication can be found elsewhere.[39] Film composition was verified using Rutherford Backscattering Spectrometry (RBS) using 1.8 MeV $^4He^+$ ions in a Cornell geometry with a dose of 4 μC. The random rotation mode was selected to minimize the substrate channeling, with the samples oriented at 5 ° with respect to the incident beam. RBS spectra were modelled using the SIMNRA simulation software.[40] A summary of the main deposition parameters, sample composition and film thickness is shown in Table I.

The optical properties and film thickness were determined by Variable Angle Spectroscopic Ellipsometry (VASE) using a J. A. Woollam M-2000 UV-Vis ellipsometer with near-infrared extension. The data were acquired at 5 angles of incidence: 55°, 60°, 65°, 70° and 75°. Measurements were taken from 250 nm up to 1700 nm, with a step of 1.5 nm. Experimental data was modelled with the J. A. Woollam's CompleteEASE™ software package assuming a single homogeneous layer with surface roughness on a Si substrate.[41] Non-absorbing films were modelled using a Cauchy dispersion relation. On the contrary, three different models were sequentially applied to absorbing films: a Cauchy dispersion relation, a B-spline model with complex refractive index, and finally a Kramers-Kronig consistent parametric model using a Tauc-Lorentz oscillator. Best simulated parameters were adjusted through minimization of the mean-square error between model and experiment (MSE < 6 in all cases). Photoluminescence (PL) emission of samples was obtained under continuous-wave external lasing excitation at 325 nm with a He-Cd laser, with an average laser power of 10 mWSpectra were recorded with a charge-coupled device spectrometer with a resolution of 0.1 nm. Chromaticity coordinates were obtained using the BenWin+ software. Cathodoluminescence (CL) measurements were carried out on a FE-scanning electron microscopy (SEM) equipped with a high resolution spectrometer

coupled to an objective that is placed at a working distance of 1.2 cm from the sample. An electron beam of 20 keV with a current value of 36 nA was used as excitation source.

Film morphology was inspected by high-resolution transmission electron microscopy (HRTEM) using a JEOL 2010F TEM operating at 200 keV. Samples were preliminarily prepared by mechanical polishing. Deposition and patterning of transparent conductive electrodes was carried out in an Electron Beam Physical Vapour Deposition (EB-PVD) system with no additional O_2 incorporation and using a shadow mask configuration. Commercial indium tin oxide (ITO) pellets (90 % In_2O_3, 10 % SnO_2) were used as deposition targets. A mean deposition rate of 1 Å·s^{-1} was established, with a final nominal thickness of 200 nm and an average transmittance of 90 % in the visible range. Further details of this approach can be found in ref. 42. The microstructure of deposited ITO electrodes was determined by X-ray diffraction (XRD) using the Cu Kα radiation (1.540598 Å) in the 0-80° range with a step size of 0.026° and a holding time of 100 s. The tube voltage and current were 45 kV and 40 mA, respectively. The surface topography of the ITO electrodes was resolved by confocal microscopy. A semiconductor device analyzer connected to a high-precision probe station and coupled to an optical detection system composed by a near field objective, a grating spectrometer and a cryogenically cooled charge coupled device was used for the optoelectronic characterization of thin films.

III. RESULTS AND DISCUSSION

The study of deposited films was performed according to the following methodology: At first, the layer composition and optical properties of RE-doped thin films containing single luminescent species (either Ce^{3+} or Tb^{3+}) were studied by means of RBS and VASE measurements (sections A and B), followed by the study of the PL characteristic and the HRTEM characterization of selected samples (sections C and D). Later on, the best fabrication parameters that yield superior luminescence of thin films were chosen and used to fabricate RE co-doped thin films and multilayers with two different dopants, i.e. Ce^{3+} and Tb^{3+} (section E). Finally, after a preliminary characterization of their optical properties and morphology by means of PL and HRTEM measurements, the suitability of these RE-doped thin films to be used as active elements in electrically driven light sources was tested by depositing a series of transparent electrodes over selected samples to obtain a general overview of their optoelectronic properties (section F).

A. Rutherford Backscattering Spectrometry

The fabrication procedure explained in the previous section allowed us to obtain a set of samples with a gradual variation of layer composition from a nearly stoichiometric SiO_2 (~ 33 at. % of Si and ~ 67 at. % of O) to a SiO_xN_y (~ 35 at. % of Si, ~ 22 at. % of O and ~ 42 at. % of N) that was confirmed by RBS analysis. Notice that since the Si content remains almost unchanged (from 33 at. % to 35 at. %), the characterization of samples will be performed based on the nitrogen content in the

samples, at the expense of oxygen. A RE doping concentration of around 1 at. % was measured in all samples. It is worth noting that such values did not suffer important changes upon different annealing temperatures. Figure 1 (a) shows representative RBS data of two Tb^{3+}-doped samples with different layer compositions. Notice the Tb peak located at high energy values (around of 1600 keV). Also, a low energy background is observed for energies below 950 keV that corresponds to the backscattering from Si nuclei located at the substrate (marked with a vertical arrow in figure 1(a)). Moreover, several peaks appear superimposed on the background Si signal that belong to the remaining constitutive elements of the deposited film, i.e. O and N (also marked in figure 1(a)). Such signal overlap between the Si substrate and the compositional elements puts forward the importance of the substrate in RBS analysis to fully exploit the results. Thus, optimum resolution is obtained for targeted materials composed of 'heavy' elements deposited on 'light' substrates with lower atomic numbers. In this case, however, and despite the overlap displayed in O and N elements, a fairly good estimate of layer composition was obtained since overlapping signals were well-resolved above the substrate background in all cases. Similarly, the Si signal shows a well-resolved double step-like decay of the number of counts around 1000 keV attributed to a transition in the Si signal produced by the combination of two different phenomena; (i) the different density of Si nuclei between the deposited thin film and the Si substrate; and (ii) the fact that back-reflected ions colliding with Si nuclei in the substrate have already lost more energy by electron scattering than the ones reflected by Si nuclei belonging to the deposited film. This is considered as a thickness-dependent effect since it becomes more evident for thicker films and also produces the broadening of the RBS signal for a particular element due to the electronic stopping. Indeed, it could be used to approximately determine the layer thickness of a particular sample, provided that such value is lower than the physical penetration limit (around ~ 2 μm for $^4He^+$ ions).

A comparison between normalized Ce- and Tb-related RBS signals is displayed in Figure 1(b). As can be observed, Tb RBS signal is centered at higher energy values than the Ce signal. This fact agrees well with the theory of RBS analysis,[43] since the relative energy loss of the back-reflected signal with regard to the incident beam is expected to decrease for higher atomic numbers of the targeted element. Thus, the fact that the back-reflected energy spectrum from Tb nuclei is closer to the value of the incident beam (1800 keV) than the one of Ce is justified by the difference in atomic numbers between both elements (Z = 65 for Tb and Z = 58 for Ce). Moreover, the relatively flat tops of the Tb and Ce spectra in figure 1(b) also indicates a fairly homogeneous distribution of RE elements along the entire depth profile, which is desirable from the optoelectronic viewpoint.

B. Variable Angle Spectroscopic Ellipsometry

Figure 2 shows the most relevant features extracted from VASE analysis (color bar scales) as a function of the annealing temperature (x-axis scale) and the nitrogen atomic percentage (y-axis scale). In particular, figure 2(a) depicts the measured layer thickness for the studied set of samples. It is worth to mention that marginal sample roughness was found in all cases,

with a mean value below 2 nm. A clear layer shrinkage is observed upon oxygen by nitrogen replacement in the matrix (for a deposition time of 1 h in all samples), denoting higher density in SiO_xN_y films compared to SiO_2, as expected .[44] A relative shrinkage of about 25 % was measured compared to the as-deposited SiO_2 reference layer. Similarly, a moderate reduction of the effective layer thickness up to 5 % is observed for increasing annealing temperatures. In this latter case however, we attribute such thickness shrinkage to an effective reduction of voids via thermally-activated desorption of H from the matrix since no remarkable variation in composition was measured in RBS analysis for as-deposited and annealed samples. [45]

Figure 2(b) displays a color map of the measured refractive index (n) at 632.8 nm, with the expected linear dependence between the increase of the nitrogen content in the matrix and n.[46] The values for n range from 1.5, close to the one typically reported for SiO_2, up to 1.8 for the maximum nitrogen content (42 at. %). Indeed, this last value is close to the optimum one (n ~ 1.75) for a stress-compensated layer.[47] On the other hand, the marginal dependence of n on the annealing temperature denotes a stable layer composition when samples are subjected to different annealing temperatures.

Similarly, figure 2(c) presents the dependence of the fundamental absorption band edge (E_g) of samples on the annealing temperature and the nitrogen content, respectively. The Tauc rule for indirect band gap materials was used to extract the optical band gap:[48]

$$h\nu \propto (\alpha h\nu)^{1/2} + E_g \,. \tag{1}$$

where $h\nu$ is the photon energy and α is the absorption coefficient, i.e. $\alpha = 4\pi k/\lambda$. Notice that the y-axis scale starts at a nitrogen content of 10 % instead of 0 % (as is the case for figures 2 (a) and (b)) since layers with lower N concentration did not show any measurable absorption in the UV range, hence having an optical gap greater than 5 eV. For the absorbing films, a gradual red-shift of the absorption edge was observed upon increase of the nitrogen content in the SiO_xN_y matrix, as expected.[37] The increase of the annealing temperature, however, seems to trigger the opposite effect, hence producing a blue-shift in the band edge absorption most probably due to the effective passivation of thin films.

C. Photoluminescence

The study of the PL emission as a function of both the atomic nitrogen content in the matrix and the annealing temperature proved particularly interesting, especially for Ce^{3+}-doped films. Being a parity allowed transition, the emission of Ce^{3+} ions from $5d^1$-to-$4f^1$ states becomes strongly dependent on the local coordination with its surrounding environment (nepheulaxetic effect). Thus, the gradual replacement of oxygen by nitrogen is expected to affect the luminescence properties of Ce^{3+}-doped films. Tb^{3+} emission, on the other hand, is governed by a parity forbidden intra-4f transition, providing weak interaction with the environment and therefore, marginal dependence on the layer stoichiometry is anticipated. Figure 3 displays the color map

panels of the normalized integrated PL emission of Ce^{3+}- (panel (a)) and Tb^{3+}-doped (panel (b)) films. In order to perform a qualitative comparison between samples, the PL emission was normalized by the layer thickness and also by the collected light fraction of emitted power radiated as a function of the refractive index of each sample, assuming a Lambertian emission. All samples showed intense PL emission easily observable by the naked eye under daylight conditions regardless of the annealing temperature (even as-deposited samples). However, an annealing treatment is normally performed to increase the Ce^{3+}/Ce^{4+} ratio (Ce^{4+} ions do not contribute to the PL emission) and to passivate the film by removing non-radiative centers.[49] Interestingly, the PL emission of Ce^{3+}-doped films shows a stronger dependence on the nitrogen content and the annealing temperature than the one measured from Tb-doped samples, in which intense PL is observed over a broader range of parameters. In particular, the PL from Ce^{3+}-doped samples is optimized when either (i) an annealing temperature between 800 °C and 1000 °C is applied, if the nitrogen atomic percentage no larger than 20 %, or (ii) at very high annealing temperatures (1180 °C) with the nitrogen concentration exceeding 30 at. %. On the contrary, Tb^{3+}-doped samples (figure 3(b)) show intense PL emission for nitrogen contents from 10 to 42 at. % and for annealing temperatures between 400 °C and 1180 °C. Another remarkable point is presented through the insets of figures 3(a) and (b), where a representative PL-T characteristic of two films containing different nitrogen content is compared (5 and 40 at. %, respectively). As can be observed, the PL-T profile of the $Ce^{3+}(Tb^{3+})$:SiO_xN_y films with N = 5 at. % (green line) presents a maximum PL intensity at 900 °C in both cases, with a gradual decrease for increasing annealing temperatures up to 1100 °C, followed by a partial recovery of the PL for even higher values up to 1180 °C. Such decrease of the PL emission has been commonly associated with the partial clustering of RE ions,[24] whereas the emergence of PL at very high temperatures may be a consequence of the formation of RE silicates that are known to emit an intense luminescence signal.[50] On the contrary, the PL-T characteristic of the $Ce^{3+}(Tb^{3+})$-doped nitrogen-rich sample (N = 40 at. %) exhibits an ever increasing trend with an integrated PL emission at 1180 °C that is twice the best one measured at 900 °C for the sample with N = 5 at. %. Thus, in general, nitrogen incorporation provides a more favorable local environment for RE ions, as brighter PL emission is obtained.

An interesting point of discussion, bearing in mind the energy at which Ce^{3+}- and Tb^{3+}-doped films are excited, i.e. ~ 3.8 eV, is the main excitation mechanisms of such RE ions. With the pumping energy being resonant with the UV absorption band of Ce^{3+} ions, a direct excitation from the fundamental level $^2F_{5/2}$ up to the 5d states is expected to dominate, regardless of the nitrogen content.[51] For Tb^{3+} ions however, no absorption bands are located at the pumping energy,[52] and thus, indirect excitation is expected. Indeed, if we recall how the nitrogen incorporation modifies the measured energy bandgap of samples (see figure 2(c)), we find a range from ~ 4.2 eV for nitrogen-free SiO_2 hosts down to ~ 3.6 eV for a nitrogen content of 42 at. % in SiO_xN_y films. At this point, we propose two different energy transfer processes occurring in our Tb^{3+}-doped samples that mostly depend on the material bandgap; (i) for excitation pumping energies larger than the bandgap, carrier mediated excitation from the

extended states to Tb^{3+} ions predominates,[52] while (ii) for pumping excitation energies smaller than the measured bandgap, the energy transfer from band tail energy states (Urbach states) to Tb^{3+} ions governs the luminescence.[53] Moreover, such intraband energy transfer is expected to gain relevance for large bandgap hosts (SiO_2), where the Urbach energy becomes higher.[37] A more accurate modeling of ellipsometry measurements using a Codi-Lorentz dispersion function instead of a Tauc-Lorentz expression is required to provide a first estimation of the Urbach absorption tails at energies below E_g.[41]

Another remarkable consequence of the increase of nitrogen in the matrix is the gradual red-shift of the PL spectra observed in Ce^{3+}-doped films.[54] As was explained before, the 5d states of Ce^{3+} ions strongly interact with the surrounding media and consequently, as the luminescence is dominated by radiative 5d-to-4f transitions, modify the emission properties according to the local environment. This effect can be observed in figure 4(a), where the peak position of the PL spectra is represented as a function of the annealing temperature and the nitrogen content. As expected, the PL spectra can be shifted by increasing either the nitrogen content or the annealing temperature. A maximum red-shift of 76 nm was measured, with an initial PL peak position of 400 nm for nitrogen-free samples. Figure 4(b) shows three illustrative PL spectra of Ce^{3+}-doped samples with gradual red-shift. Notice that apart from the broad PL emission around 400-476 nm, which is associated with Ce^{3+} radiative transitions, a much narrower doublet corresponding to Tb^{3+} emission was also measured at ~ 545 nm. Thus, such emission provides an unambiguous fingerprint of the presence of Tb^{3+} ions in the matrix, and indicates a residual cross-contamination of the deposition chamber. Nevertheless, the fact that no Tb incorporation was measured by RBS in Ce^{3+}-doped films limits such contamination to atomic percentages lower than the resolution limit of the RBS equipment, i.e. below 0.1 %. Surprisingly, the PL emission of both RE ions became comparable in intensity in a few samples in spite of the fact that there is significantly more Ce incorporated compared to Tb (at least one order of magnitude, 1 % versus < 0.1 %). A comprehensive explanation is that a non-negligible percentage of Tb^{3+} ions is being sensitized by Ce^{3+} ions, which will absorb and deliver part of the excitation energy efficiently. Indeed, such effect was already observed in similar samples containing Ce silicates and Tb^{3+} ions.[55] In our case however, we cannot discard such sensitization process to be also led by Ce^{3+} ions outside of Ce silicates, as in oxyfluoride aluminosilicates,[56] since strong Tb^{3+} emission was also observed in Ce^{3+}-doped films annealed at lower temperatures (700 - 800 °C), where Ce silicate formation does not take place. Despite the unexpected emergence of the Tb^{3+} peak in Ce^{3+}-doped films, its role in the luminescence properties is marginal in most of the analyzed samples (much weaker emission compared to the one of Ce^{3+} ions) and therefore it will be disregarded from this point on. Moreover, it should be noted that we did not measure any narrowing of the Ce^{3+} PL emission for samples annealed at 1180 °C. Progressive narrowing of the Ce^{3+} emission (and therefore a better color rendering) is foreseen for samples subjected to increased thermal budgets due to the sequential formation of Ce silicates with a stable bonding structure, as in ref. 57. In that work, spectral narrowing PL emission from Ce silicates was only seen after 3 h annealing at 1200 °C.

Concerning Tb^{3+}-doped films, the analysis of the PL peak position as a function of the studied parameters presents an almost flat dependence since the emission is dominated by inner radiative transitions (intra-4f states) and therefore, the influence of the environment on the emission is rather negligible in this case.

D. Transmission Electron Microscopy

HRTEM characterization was performed in selected films to provide evidences of the clustering of RE ions at high annealing temperatures and also to confirm the presence of RE silicates. Figure 5 shows the main results of this study in a representative Ce^{3+}-doped SiO_2 film annealed at 1180 °C. Randomly distributed Ce clusters with mean diameter of ~ 5 nm are observed in figure 5 (a), corroborating our previous hypothesis. Moreover, a Fast Fourier Transform (FFT) was performed over a single Ce cluster (the area is marked with a red square), showing an amorphous morphology. Thus, the progressive degradation of the PL signal for annealing temperatures beyond 900 °C in samples with low nitrogen content can be unambiguously attributed to the formation of non-emitting amorphous Ce clusters. In addition, crystalline silicate phases were also observed at specific sites of the sample. In particular, relatively large crystalline Ce silicates with lengths of a few tenths of nanometers were identified at the substrate-active layer interface, as shown in the HRTEM image in figure 4(b). In this case, the FFT performed over such Ce crystallites showed a crystalline morphology with a lattice constant of ~ 0.2 nm, in agreement with previously reported works.[51] Therefore, the emergence of the PL emission from either Tb^{3+}- or Ce^{3+}-doped films at high annealing temperatures can be attributed to the formation of RE silicates. Such nanocrystallites provide an ideal trivalent bonding for RE ions, which are evenly distributed within the crystal. Two different silicate phases are expected: $Ce_2Si_2O_7$ or $Ce_{4.667}(SiO_4)_3O$.[57] Moreover, a remarkable decrease of the RE clustering (in both amorphous and crystalline phases) was observed in nitrogen-rich SiO_xN_y samples, indicating a higher solubility limit for RE ions upon replacement of oxygen by nitrogen in the host.

E. Rare Earth Co-doping: Single Vs Multilayer Approach

Apart from the single RE doping, the study of RE co-doped SiO_xN_y films with a smart design configuration is also interesting, as such films could lead to the development of bright samples with wide color tunability. For that however, one should take into account the ion-ion interactions, especially for the case explained above, in which Ce^{3+} ions assist Tb^{3+} luminescence via efficient sensitization. Although such an effect is generally of high interest as it yields considerable improvement of the PL emission of Tb^{3+} ions, it also quenches almost completely the PL emission from Ce^{3+} ions, hence compromising the color mixing. Therefore, a new set of samples based on the multilayer approach was designed to minimize such effects. In particular, three new designs were explored using the matrix composition with the highest nitrogen atomic concentration: (i) a Ce^{3+} and Tb^{3+} co-doped SiO_xN_y single layer, (ii) a bilayer composed of a Ce^{3+}-doped SiO_xN_y layer

deposited on top of a Tb^{3+}-doped SiO_xN_y, each one 30 nm thick and (iii) a multilayer based on two Ce^{3+}-doped SiO_xN_y layers and two Tb^{3+}-doped SiO_xN_y layers, each 15 nm thick and separated by SiO_2 barriers of 5 nm. Each RE-doped film has an average RE concentration of 1 at. %, equal to the previous batch of samples. Figure 6(a) displays a schematic cross-section of each design. Whereas Ce^{3+} and Tb^{3+} ions are randomly distributed within the film in the first approach, the latter two provide a physical separation between them. Notice that the effective thickness of emission layer is the same in all cases, around 60 nm. The structure of each approach was validated by TEM measurements, revealing features in agreement with the proposed designs, as seen in figure 6(b). Remarkably, neither waviness nor layer mixing is observed. In addition, the fact that the morphological structure remains unaltered even after annealing at 1180 °C for 1 h validates the fabrication process and suggests the robustness of samples (see inset of figure 6(b)). Moreover, the emergence of RE clustering under high thermal budget seems to be marginal in the multilayer approach, in accordance with previous works that already report on the absence of clustering in RE-doped multilayer-based samples containing either Er or Tb dopants.[42,58]

Figure 7 shows the PL characterization of RE co-doped samples as a function of the annealing temperature, with Figure 7(a) being the one corresponding to the single layer, Figure 7(b) the bilayer and finally Figure 7(c) representing the multilayer approach. Focusing on the single layer first, we observe two different trends for Tb^{3+} and Ce^{3+} peak emissions. Whereas the emission of the Ce^{3+} peak remains almost constant or suffers a rather moderate improvement with the annealing temperature, the emission of Tb^{3+} shows strong increase from 800 °C on. Indeed, at the maximum annealing temperature, the emission of the Tb^{3+} main peak is of about one order of magnitude higher than that of Ce^{3+}. This effect can be understood as an indirect fingerprint of the interaction between optically active Ce^{3+} and Tb^{3+} dopants, and more precisely of the energy transfer between them. Furthermore, we can distinguish between two different regimes depending on the annealing temperature: for an annealing temperature up to 1000 °C, the energy transfer is moderate and so is the PL enhancement of the Tb^{3+} peak with regard to Ce^{3+} emission; on the other hand, the Tb^{3+} emission increases dramatically for higher annealing temperatures, presumably as a consequence of a more efficient sensitization of Tb^{3+} ions. Indeed, considering the range of annealing temperatures at which the onset occurs, it seems reasonable to assume that the energy transfer becomes remarkably more efficient when Tb^{3+} ions are sensitized by Ce silicates that have formed during the annealing treatment. As a consequence, the PL line shape of the sample becomes gradually changed for increasing annealing temperatures, as seen in the inset of figure 7(a). Interestingly, this situation no longer applies for the two other configurations (the bilayer and the multilayer) displayed in figures 7(b) and (c) that show an even increase of the Ce^{3+} and Tb^{3+} PL emission, suggesting that the ion-ion interaction can be neglected for these samples, as expected. Although the difference is rather subtle, we can also differentiate between the approaches II and III, since partial saturation of Ce^{3+} emission under high annealing temperature is only observed in the RE co-doped bilayer in which SiO_2 spacers were not defined. Therefore, the sequential stacking of single doped RE-SiO_xN_y layers separated by SiO_2 barriers

seems to be the most promising design that yields strong luminescence from both RE ions. Thus, a suitable scenario to develop RE-doped luminescent thin films with wide color tunability is foreseen, just by adjusting the thickness of each RE-doped film. Indeed, such an effect was already observed for the current set of samples for the different annealing temperatures. Hence, depending on the fabrication conditions, the color of emission can be swept from the cobalt blue emission typical for Ce^{3+} ions up to the emerald green of Tb^{3+}. This situation is depicted in figure 8(a), where the XYZ coordinates of the PL emission of different samples are represented in the CIE chromaticity diagram. As can be seen, the change in chromaticity coordinate follows a linear trend in the CIE diagram that varies according to the contribution of each luminescence peak. Also, the PL emission of representative samples under room lighting conditions is shown in figures 8(b), (c) and (d) to better illustrate the variation of the color of emission with the fabrication parameters studied in this work.

F. Optoelectronic characterization

In order to gain further insight into the luminescence properties of RE-doped thin films and to validate their implementation in electroluminescent devices, a series of test devices were fabricated. For that, selective ITO deposition was performed over thin films to define the top contact, while covering the backside of the sample with Al to be used as a back contact (see section II for further information). As can be observed in figure 9(a), where a top view of a single ITO electrode is shown, the selective ITO patterning technique seems to be reasonably accurate, resulting in a well-defined and compact ITO electrode. Also, the zoom-in image of figure 9(b) denotes a granular structure, with a mean grain diameter of about 100 nm, similarly to that reported elsewhere.[59] In addition, the ITO electrodes present a polycrystalline morphology that was confirmed by XRD measurements, showing several diffraction peaks at specific angles that correspond to the different crystallographic planes (see figure 9(d)). Moreover, the height profile and surface topology of a single ITO electrode was inspected by optical interferometry, revealing an ITO thickness in accordance with the nominal value, of around 200 nm, a fairly abrupt contour, and a surface roughness of about 25 nm (figures 9(c) and 9(d)). In view of the reasonably good quality of the deposited electrodes, a preliminary optoelectronic characterization was performed over three different samples: a Tb-doped SiO_2 single layer, a Ce-doped SiO_xN_y single layer with the highest nitrogen atomic concentration and a Ce^{3+} and Tb^{3+} co-doped multilayer (approach III in figure 6(a)). 10 different devices from each sample were characterized in order to have better statistics. The main results are summarized in figure 10. Figures 10(a), (b) and (c) show the EL spectra under constant current polarization for the analyzed devices, revealing a spectral line-shape in agreement with the emission of the radiative transitions in Tb^{3+} and Ce^{3+} ions, respectively. Moreover, the CL spectrum of the ML approach is also shown in panel (c) for comparison, showing very similar emission lines that point to a RE emission pattern that is independent of the excitation source (a very similar spectral line-shape was also observed in PL measurements). Concerning the excitation mechanism of RE ions under electrical pumping, direct impact excitation of hot electrons with energies above the conduction band has been typically reported as the

most plausible mechanism in RE-doped silicon oxides and silicon oxynitride thin films[5,29,58], although the energy transfer from the matrix to RE ions via carrier mediated excitation cannot be completely ruled out.

A first inspection of the main charge transport mechanisms was carried out by means of the J-E characteristic of samples, as seen in figure 10(d). A forward-reverse sweep from 0 to 8 MV/cm was performed, with steps of 0.01 MV/cm (quasi-static sweep). As all measurements are shown in absolute values, we shall mention that devices were polarized with negative voltages over the top electrode, hence forcing a constant top-down electron flow, with a negligible hole contribution in the opposite direction (N^{++} Si substrates). Interestingly, devices containing a nitrogen-rich active layer (i.e. Ce:SiO_xN_y and Ce/Tb ML) show an electric field threshold for conduction (at 2.5-3 MV/cm) that is around of 2 MV/cm lower than in devices containing a nitrogen-free active layer (device Tb:SiO_2), where the threshold occurs at 4.5-5 MV/cm. Thus, the inclusion of nitrogen in silicon oxide thin films provides a considerable improvement of the conductivity by generating new intraband trapping sites.[29] Noteworthy, the J-E characteristic of the RE co-doped multilayer is located between the one of Tb:SiO_2 (sample with the lowest conductivity) and Ce:SiO_xN_y (sample with the highest conductivity). This behavior seems reasonable when bearing in mind that the multilayer is a mix of low (SiO_2) and high (SiO_xN_y) conductive sub-layers. Nevertheless, we shall emphasize that such reasoning does not always apply, especially for samples with considerably larger number of stacked sub-layers, since the role of the interfaces, and more particularly of the interfacial trapping sites, starts gaining relevance to the conductivity. Indeed, this was the case for sub-nanometer Tb-doped SiO_x/SiO_xN_y superlattices, where trapping sites at the interface were believed to be decisive in charge transport.[42] In our case however, the number of periods is lower and the deposited sub-layers are considerably thicker than in the superlattice (4 periods of 15/5 nm instead of ten periods of 0.7/0.9 nm), hence limiting the influence of the interfaces on the charge transport.

Two main compact models successfully reproduced the experimental J-E curves of single RE doped devices: trap-assisted tunneling with an average trap energy of ~ 2.0±0.5 eV predominates in Tb:SiO_2 devices, while Poole-Frenkel conduction governs charge transport in Ce:SiO_xN_y devices, with a relative permittivity of ~ 7±1. These results are in agreement with our expectations, as the charge transport in SiN_x and SiO_xN_y thin films is normally governed by the number of available trapping sites in the host, whereas the nearly stoichiometric SiO_2 thin film is a rather low defect density material which makes the charge transport to be mostly governed by tunneling events.[60] With regard to the RE co-doped multilayer, a combination of charge transport conduction between SiO_x and SiO_xN_y is expected, although the P-F conduction model was the one that displayed the most accurate fitting of J-E curves, with a relative permittivity of ~ 6±1. This value is plausible when bearing in mind the relative permittivity of SiO_2 ($\varepsilon_r \sim 4$) and Si_3N_4 ($\varepsilon_r \sim 7$). Notice that there is a relatively large variation of fitting parameters from one device to another, which has been attributed to the simplicity of fabricated test devices. Better homogeneity in the J-E characteristic of samples is expected for devices fabricated using the standard CMOS process, with a well-defined field oxide

spacer to limit crowded currents and device cross-talks, a protecting SiO_2 (or Si_3N_4) layer to isolate devices from the environment and by defining a metal ring in the contour of ITO electrodes to guarantee uniform current injection. Still, the optoelectronic characterization of the studied test devices is worthy as it provides a good estimation of the electro-optic performance of deposited films using a simplistic fabrication process, with no need of optical lithography nor etching processes that commonly require several steps and the use of hazardous solvents.

Interestingly, no direct correlation was found between the measured current and the area of the electrodes. Such lack of correspondence between the current and the device area is often used as a proof of the formation of filamentary currents in switching memory devices.[61] In that scenario, our thin films would display filamentary currents that show at least one discontinuity (most probably several), since either trap assisted tunneling (TAT) conduction or P-F charge transport was previously identified in the J-E characteristic. Therefore, the conductive pathways would be broken at specific sites inside the active layer, creating dielectric barriers for electrons that would be surpassed either by tunneling (TAT) or by defect-assisted conduction from neighboring defect sites (P-F). Indeed, a similar model based on discontinuous filamentary currents assisted by TAT mechanisms has already been reported in resistive switching devices containing off-stoichiometric SiO_x thin films.[62] Based on these results, we assume a similar phenomenon in our devices.

Finally, in order to further corroborate our hypotheses, a reliability test was carried by means of the constant current stress method.[63] For that, a selected current density is applied (a value that yields a measurable EL signal) while measuring the V-t characteristic, as seen in figure 10(e). The EL-t was also monitored simultaneously, although it is not shown here as it displayed an almost constant value over time until the device breakdown. The observed increase of voltage over time is characteristic of thin dielectric films and denotes a progressive charge trapping due to subsequent creation of new trapping sites. Indeed, such gradual trapping generation is believed to be one of the primary reasons of the hard breakdown in thin dielectric films.[64] In our test devices, the breakdown takes place after ~ 3200 seconds of continuous operation, as noted by the abrupt voltage drop in figure 10(e). From this point on, devices displayed a permanent low-resistive state with no measurable EL signal that confirm the irreversible damage induced in the film. Indeed, such degradation is clearly evidenced on the surface topology of the ITO electrode, showing 'burned' conductive pathways around the area of the contact point (see image I at the inset of figure 10(e)). Such permanent fingerprint, which is believed to be a consequence of the elevated joule heating of the passing current density across the ITO electrode, proves the existence of filament currents in our devices. Thus, the timing of the device breakdown strongly depends on the ability to form low-resistive percolation pathways by interconnecting randomly distributed trapping sites along filaments.[65] Remarkably, the damaged region occurs only at local level, since both the high resistive state and the EL signal are partially restored when moving the polarization tip far away from the burned zone. Thus, the new contact point provided similar optoelectronic properties than pristine devices for a few hundred of seconds, after which a new burned zone

was defined (see image II at the inset of figure 10(e)). Interestingly, the conductive filament traces seem to link with the former ones produced at the first contact point. To further corroborate this phenomenon, the process was repeated one more time, placing the polarization tip at a third different position. This time, although the high resistive state was partially recovered for a short period of time, it rapidly switched to the low-resistive state after few seconds, showing a very similar burned zone around the contact point that also links with previously damaged regions. This behavior is expected on the basis that filament currents are preferably formed around weak points where the conductivity is higher (probably due to a higher defect density), as is the case for the burned regions around contact points I and II. Interestingly, the timing of the local breakdown shortens for subsequent polarizations at different contact points, suggesting the enhanced degradation of the active layer. Another important point that deserves some attention is how the joule heating affects the quality of the ITO electrode after each local breakdown. From visual inspection, it seems reasonable to assume that the electrical and optical properties of ITO change when the active layers switch to a low-resistive state. As a first approximation, it could be considered that the ITO is being subjected to an additional high temperature annealing at specific sites caused by the joule heating dissipation of filament currents. As a consequence, the resistivity of the ITO electrode would increase accordingly, providing an additional resistance to the device. This fact was confirmed by measuring the J-E curve after the local breakdown (which displayed an ohmic-like behavior) and extracting the resistivity value assuming perfect conductive filaments (resistivity of the thin film ~ 0), that being around one order of magnitude higher than the resistivity of pristine ITO layers measured using the Van de Pauw method. Noticeably, the measured resistivity from the J-E curve also accounts for the resistivity of the bottom electrode, which may also play an important role (the resistivity of an Ohmic J-E curve is limited by the resistance of the two metal contacts). Nevertheless, and since the resistivity of the bottom contact (Al) is markedly lower than the one measured for the ITO contact, we expect such increase to be mostly due to the increase of the ITO resistivity. Further analysis focused on the microstructure and morphology is required to provide a more detailed picture of the main properties of the ITO electrodes after stress polarization.

IV. CONCLUSIONS

The suitability of Ce^{3+}- and Tb^{3+} co-doped SiO_xN_y thin films as active layers in electrically driven Si-based light sources has been assessed. Thin films were deposited in an ECR-PECVD system with in-situ RE doping capability. Luminescence of samples containing a single RE dopant was first optimized based on two primary fabrication parameters: the annealing temperature (from 500 °C up to 1180 °C) and the nitrogen atomic percentage of the SiO_xN_y compound. Departing from a nearly stoichiometric SiO_2, the nitrogen incorporation was gradually increased up to 42 at. %, at the expense of the oxygen atomic concentration, while maintaining the Si content virtually constant at around 33 at. %. Bright PL emission, easily

observable with naked eyes in daylight conditions, was obtained from all samples when excited upon UV laser excitation at 325 nm. Noticeably, the PL intensity became considerably improved when performing moderate-high annealing temperatures and by introducing high nitrogen contents (42 at. %) in the host. In that regard, the emission from Ce^{3+} ions proved to be more sensitive to the studied parameters than Tb^{3+}. In particular, Ce^{3+} emission was maximized either for a nitrogen percentage lower than 20 at. % and an annealing temperature range of 800-1000 °C, or for a high nitrogen percentage (42 at. %) and a high annealing temperature (1180 °C). In turn, Tb^{3+} emission displayed a more relaxed condition, with outstanding luminescence for a range of nitrogen atomic percentage spanning from 10 to 42 at. % and an annealing temperature range from 400 to 1180 °C. Ce^{3+} and Tb^{3+} co-doping of SiO_xN_y thin films was also investigated by means of three different configurations: a SiO_xN_y single layer with both RE ions randomly distributed, a bilayer composed of a Ce^{3+}-doped SiO_xN_y deposited over a Tb^{3+}-doped SiO_xN_y thin film, and a multilayer approach based on either Ce^{3+}- or Tb^{3+}-doped SiO_xN_y layers separated by interleaved SiO_2 spacers. Limited color tunability was observed in the emission of the RE-doped single layer as a consequence of the efficient energy transfer from either Ce^{3+} ions or Ce silicates to Tb^{3+} ions. As a consequence, very intense Tb^{3+}-related green emission was measured in the single layer, with negligible blue emission from Ce^{3+} species. On the contrary, both the bilayer and the multilayer presented a PL pattern that, despite being less intense than the single layer, showed independent contributions from Ce^{3+} and Tb^{3+} ions. As a consequence, a wide palette of colors in the PL emission was demonstrated just by adjusting the contribution of each luminescent species. Finally, a preliminary optoelectronic characterization was performed in selected samples to determine the suitability of RE-doped thin films to be excited under electrical pumping. For that, transparent conductive oxides (ITO) were deposited at specific sites over thin films by using a shadow mask approach. EL spectra in agreement with the radiative transitions of Ce^{3+} and Tb^{3+} ions was collected, and a correlation between the charge transport mechanism and the sample composition was performed. Moreover, the constant current stress method was implemented to further insight on the early degradation of fabricated test devices, showing a breakdown process dominated by the progressive creation of highly conductive filament currents that generate excessive joule heating at localized sites around the polarization point. Superior performance is foreseen in devices fabricated using a standard CMOS process.

ACKNOWLEDGEMENTS

This research is supported by the Spanish Ministry of Science and Innovation (TEC2012-38540-C02-01). RBS characterization was performed in the Tandetron Accelerator Laboratory at Western University in London, ON (Canada). TEM characterization was carried out in the Science and Technical Centers (CCiT) of the University of Barcelona. In Canada, this work was supported by the Natural Sciences and Engineering Research Council (NSERC) under the Discovery Grants program.

REFERENCES

[1]L. Pavesi, and D. J. Lockwood, *Silicon photonics* (Springer Science & Business Media, 2004).

[2]R. Soref, IEEE J. Sel. Topics Quantum Electron. 12(6), 1678-1687 (2006).

[3]F. Priolo, T. Gregorkiewicz, M. Galli, and T. F. Krauss, Nature Nanotech. 9(1), 19-32 (2014).

[4]L. Pavesi, and G. Guillot, *Optical interconnects* (Springer Series in Optical Sciences, 119, 2006).

[5]L. Rebohle, and W. Skorupa, *Rare-Earth implanted MOS devices for silicon photonics* (Springer Series in Materials Science, Berlin, 2010).

[6]P. J. Venter, and M. Du Plessis, J. Display Technol. 10(9), 721-728 (2014).

[7]V. S. Lin, K. Motesharei, K. P. S. Dancil, M. J. Sailor, and M. R. Ghadiri, Science 278(5339), 840-843 (1997).

[8]L. Rebohle, T. Gebel, R. A. Yankov, T. Trautmann, W. Skorupa, J. Sun, G. Gauglitz, and R. Frank, Opt. Mater. 27(5), 1055-1058 (2005).

[9]W. L. Ng, M. A. Lourenco, R. M. Gwilliam, S. Ledain, G. Shao, and K. P. Homewood, Nature 410(6825), 192-194 (2001).

[10]D. Timmerman, J. Valenta, K. Dohnalová, W. D. A. M. De Boer, and T. Gregorkiewicz, Nature Nanotech. 6(11), 710-713 (2011).

[11]D. Liang, and J. E. Bowers, Nature Photon. 4(8), 511-517 (2010).

[12]J. W. Yang, A. Lunev, G. Simin, A. Chitnis, M. Shatalov, M. A. Khan, J. E. Van Nostrand, and R. Gaska, Appl. Phys. Lett. 76(3), 273-275 (2000).

[13]R. Chen, T. T. D. Tran, K. W. Ng, W. S. Ko, L. C. Chuang, F. G. Sedgwick, and C. Chang-Hasnain, Nature Photon. 5(3), 170-175 (2011).

[14]H. Park, A. W. Fang, S. Kodama, and J. E. Bowers, Opt. Express, 13(23), 9460-9464 (2005).

[15]Y. Koninck, G. Roelkens, and R. Baets, Laser Photon. Rev. 9(2), L6-L10 (2015).

[16]J. Li, O. H. Y. Zalloum, T. Roschuk, C. L. Heng, J. Wojcik, and P. Mascher, Adv. Opt. Technol. 2008, 295601 (2008).

[17]T. J. Kippenberg, J. Kalkman, A. Polman, and K. J. Vahala, Phys. Rev. A 74, 051802(R) (2006).

[18]S. Y. Seo, and J. H. Shin, MRS Proceedings 770, I6-10 (2003).

[19]J. Sun, W. Skorupa, T. Dekorsy, M. Helm, L. Rebohle, and T. Gebel, J. Appl. Phys. 97(12), 123513 (2005).

[20]A. R. Zanatta, A. Khan, and M. E. Kordesch, J. Phys.: Condens. Matter, 19(43), 436230-436237 (2007).

[21]G. Bellocchi, F. Iacona, M. Miritello, T. Cesca, and G. Franzò, Opt. Express, 21(17), 20280-20290 (2013).

[22]C. Lv, C. Zhu, C. Wang, Y. Gao, X. Ma, and D. Yang, Appl. Phys. Lett. 106(14), 141102 (2015).

[23]L. Rebohle, M. Braun, R. Wutzler, B. Liu, J. M. Sun, M. Helm, and W. Skorupa, Appl. Phys. Lett. 104(25), 251113 (2014).

[24]N. Prtljaga, D. Navarro-Urrios, A. Tengattini, A. Anopchenko, J. M. Ramírez, J. M. Rebled, S. Estradé, J. P. Colonna, J. M. Fedeli, B. Garrido, and L. Pavesi, Opt. Mat. Express, 2(9), 1278-1285 (2012).

[25]D. Arnold, E. Cartier, and D. J. DiMaria, Phys. Rev. B, 49(15), 10278 (1994).

[26]S. Yerci, R. Li, and L. Dal Negro, Appl. Phys. Lett. 97(8), 081109 (2010).

[27]L. Xu, S. Li, L. Jin, D. Li, and D. Yang, Nanoscale Res. Lett. 9(1), 1-6 (2014).

[28]W. D. Sacher, Y. Huang, G. Q. Lo, and J. K. Poon, J. Lightw. Technol. 33(4), 901-910 (2015).

[29]D. J. DiMaria, and J. R. Abernathey, J. Appl. Phys. 60(5), 1727-1729 (1986).

[30]D. J. Moss, R. Morandotti, A. L. Gaeta, and M. Lipson, Nature Photon. 7(8), 597-607 (2013).

[31]N. Izhaky, M. T. Morse, S. Koehl, O. Cohen, D. Rubin, A. Barkai, G. Sarid, R. Cohen, and M. J. Paniccia, IEEE J. Sel. Topics Quantum Electron. 12(6), 1688-1698 (2006).

[32]K. Wörhoff, L. T. H. Hilderink, A. Driessen, and P. V. Lambeck, J. Electrochem. Soc. 149(8), F85-F91 (2002).

[33]B. Dierre, R. J. Xie, N. Hirosaki, and T. Sekiguchi, J. Mater. Res. 22(7), 1933-1941 (2007).

[34]D. K. T. Ng, Q. Wang, T. Wang, S. K. Ng, Y. T. Toh, K. P. Lim, Y. Yang, and D. T. H. Tan, ACS Appl. Mater. Interfaces, 7(39), 21884-21889 (2015).

[35]P. Zhang, K. Chen, Z. Lin, H. Dong, W. Li, J. Xu, and X. Huang, Appl. Phys. Lett. 106, 231103 (2015).

[36] G. Q. Xu, Z. X. Zheng, W. M. Tang, and Y. C. Wu, J. Lumin. 124, 151-156 (2007).

[37]M. I. Alayo, I. Pereyra, W. L. Scopel, and M. C. A. Fantini, Thin Solid Films 402(1), 154-161 (2002).

[38]A. Sassella, A. Borghesi, F. Corni, A. Monelli, G. Ottaviani, R. Tonini, B. Pivac, M. Bacchetta, and L. Zanotti, J. Vac. Sci. Technol. A 15(2), 377-389 (1997).

[39]J. M. Ramírez, J. Wojcik, Y. Berencén, P. Mascher, and B. Garrido, Spie Photonics Europe. International Society for Optics and Photonics 913309-913309-9 (2014).

[40]M. Mayer, *SIMNRA user's guide* (1997).

[41]J. Hale, and B. Johs, *CompleteEASE™ Data Analysis Manual*. Lincoln, Nebraska: J. A. Woollam Co., Inc., 2011.

[42]J. M. Ramírez, J. Wojcik, Y. Berencén, A. Ruiz-Caridad, S. Estradé, F. Peiró, P. Mascher, and B. Garrido. Nanotechnology 26(8), 085203 (2015).

[43]W. K. Chu, J. W. Mayer, and M.-A. Nicolet, *Backscattering spectrometry* (Academic Press, Inc., New York, 1978).

[44] F. H. P. Habraken, A. E. T. Kuiper, Y. Tamminga, and J. B. Theeten, J. Appl. Phys. 53(10), 6996-7002 (1982).

[45]A. E. T. Kuiper, M. F. C. Willemsen, and L. J. van IJzendoorn, Appl. Phys. Lett. 53(22), 2149-2151 (1988).

[46]D. Criado, I. Pereyra, and M. I. Alayo, Materials Characterization 50(2), 167-171 (2003).

[47] P. Temple-Boyer, B. Hajji, J. L. Alay, J. R. Morante, and A. Martinez, Sensors and Actuators 74(1), 52-55 (1999).

[48] J. Tauc, R. Grigorovici, and A. Vancu, Phys. Status Solidi (b) 15(2), 627-637 (1966).

[49]G.Q. Xu, Z.X. Zheng, W.M. Tang, and Y.C. Wu, J. Lumin. 124(1), 151-156 (2007).

[50]W. C. Choi, H. N. Lee, E. K. Kim, Y. Kim, C.-Y. Park, H. S. Kim, and J. Y. Lee, Appl. Phys. Lett. 75(16), 2389-2391 (1999).

[51]J. Weimmerskirch-Aubatin, M. Stoffel, A. Bouché, P. Boulet, M. Vergnat, and H. Rinnert, J. Alloys Compd. 622, 358-361 (2015).

[52]H. Jeong, S.-Y. Seo, and J. H. Shin, Appl. Phys. Lett. 88(16), 161910 (2006).

[53]Y. Zhizhong, L. Dongsheng, W. Minghua, C. Peiliang, G. Daoren, W. Lei, and Y. Deren, J. Appl. Phys. 100(8), 083106 (2006).

[54]L. Pavesi, and T. Rasit, *Silicon Nanocrystals: Fundamentals, Synthesis and Applications* (Wiley-VCH Verlag GmbH, Berlin, Germany, 2010).

[55]P. R. J. Wilson, Ph.D. thesis, McMaster University, Ontario, 2013.

[56]L. Zhu, A. Lu, C. Zuo, and W. Shen, J. Alloys Compd. 509(29), 7789-7793 (2011).

[57]J. Li, O. Zalloum, T. Roschuk, C. Heng, J. Wojcik, and P. Mascher. Appl. Phys. Lett. 94(1), 011112 (2009).

[58]J. M. Ramírez, Y. Berencén, L. López-Conesa, J. M. Rebled , F. Peiró, and B. Garrido, Appl. Phys. Lett. 103(8), 081102 (2013).

[59]N. Wan, T. Wang, H. Sun, G. Chen, L. Geng, X. Gan, S. Guo, J. Xu, and K. Chen, J. Non-crystalline solids, 356(18), 911-916 (2010).

[60]M. Nardone, M. Simon, I. V. Karpov, and V. G. Karpov, J. Appl. Phys. 112(7), 071101 (2012).

[61]A. Mehonic, and A. J. Kenyon, Defects at Oxide Surfaces, pp. 401-428 (Springer International Publishing, 2015).

[62] A. Mehonic, S. Cueff, M. Wodjak, S. Hudziak, O. Jambois, C. Labbé, B. Garrido, R. Rizk, and A. J. Kenyon, J. Appl. Phys. 111(7), 074507 (2012).

[63]P. P. Apte, T. Kubota, and K. C. Saraswat, J. Electrochem. Soc. 140(3), 770-773 (1993).

[64]P. P. Apte, and K. C. Saraswat, IEEE. Trans. Electron Devices 41(9), 1595-1602 (1994).

[65]R. Degraeve, G. Groeseneken, R. Bellens, J. L. Ogier, M. Depas, P. J. Roussel, and H. E. Maes, IEEE. Trans. Electron Devices *45*(4), 904-911 (1998).

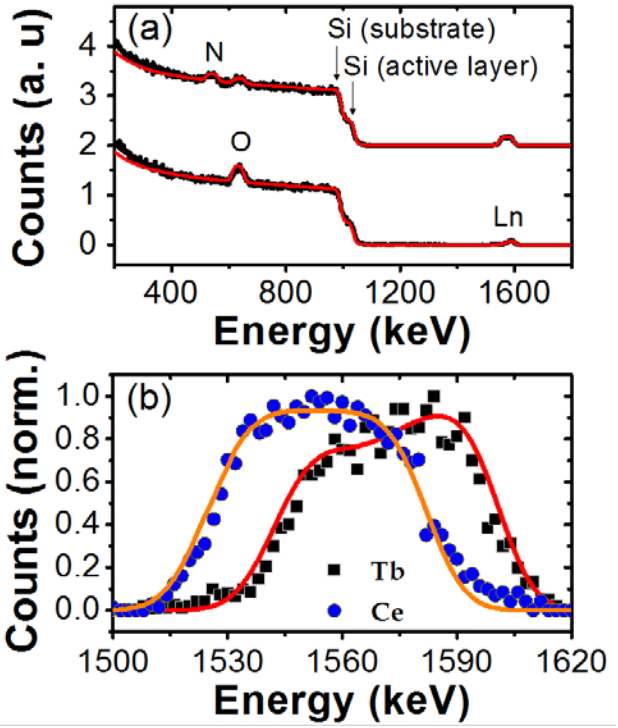

Figure 1: (a) Experimental (black line) and simulated (red line) RBS spectra of two Tb^{3+}-doped thin films with different composition. At the bottom, a SiO_2 containing 33 at. % of Si and 67 at. % of O. On top, a SiO_xN_y layer with 35 at. % of Si, 22 at. % of O and 42 at. % of N. Rare earth incorporation is around of 1 % in both samples (lanthanide peak, Ln). (b) Comparison between the normalized RBS peak of Tb (black squares) and Ce (blue dots). Overlapping red and orange curves stand for the simulated curves.

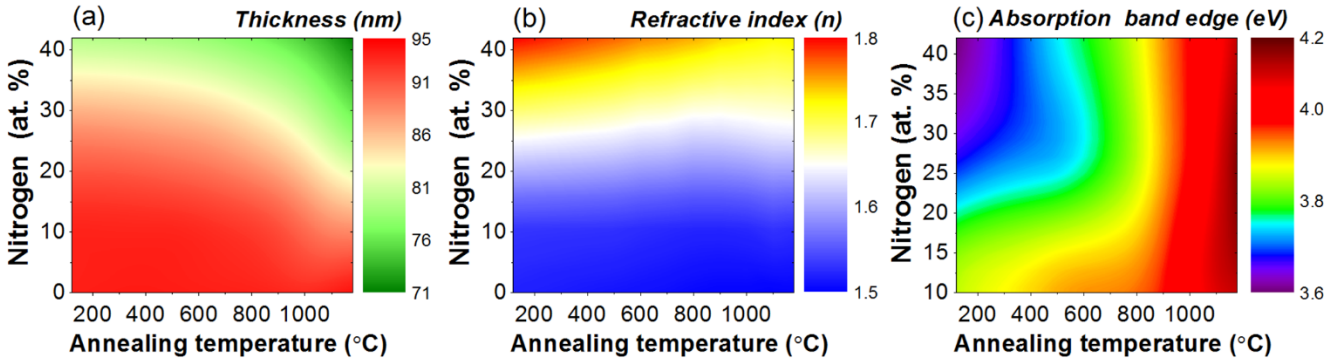

Figure 2: Color map figures of the measured thickness (panel (a)), the refractive index at 632.8 nm (panel (b)) and the absorption band edge (panel (c)) of deposited thin films as a function of the measured nitrogen content in the matrix (y-axis) and the annealing temperature (x-axis).

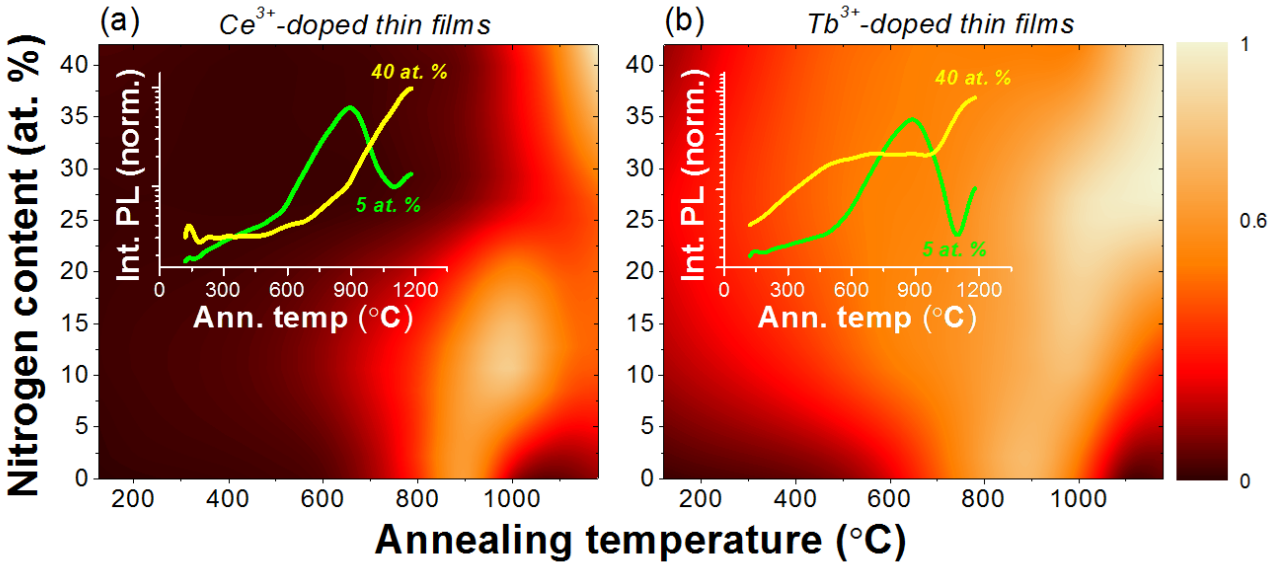

Figure 3: Normalized integrated PL intensity (color bar) of Ce^{3+}-doped (panel (a)) and Tb^{3+}-doped (panel (b)) thin films as a function of the nitrogen content (y-axis) and the annealing temperature (x-axis). The normalized color bar scale represents the PL intensity over two orders of magnitude between the sample with the poorest emission and the one with brightest PL intensity. Insets compare the integrated PL intensity of samples containing different nitrogen concentration (either 5 at. % or 40 at. %) as a function of the annealing temperature.

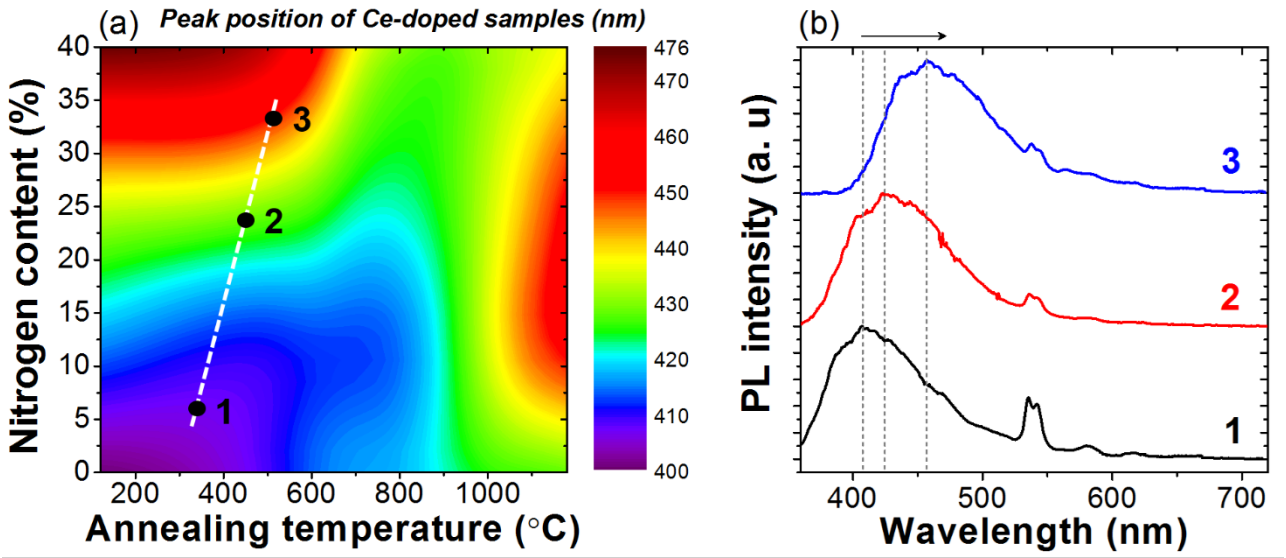

Figure 4: (a) color map figure of the peak position of Ce^{3+} emission (color bar) as a function of the nitrogen content (y-axis) and the annealing temperature (x-axis). (b) Representative PL spectra of different Ce^{3+}-doped thin films located along an imaginary straight-line in panel (a).

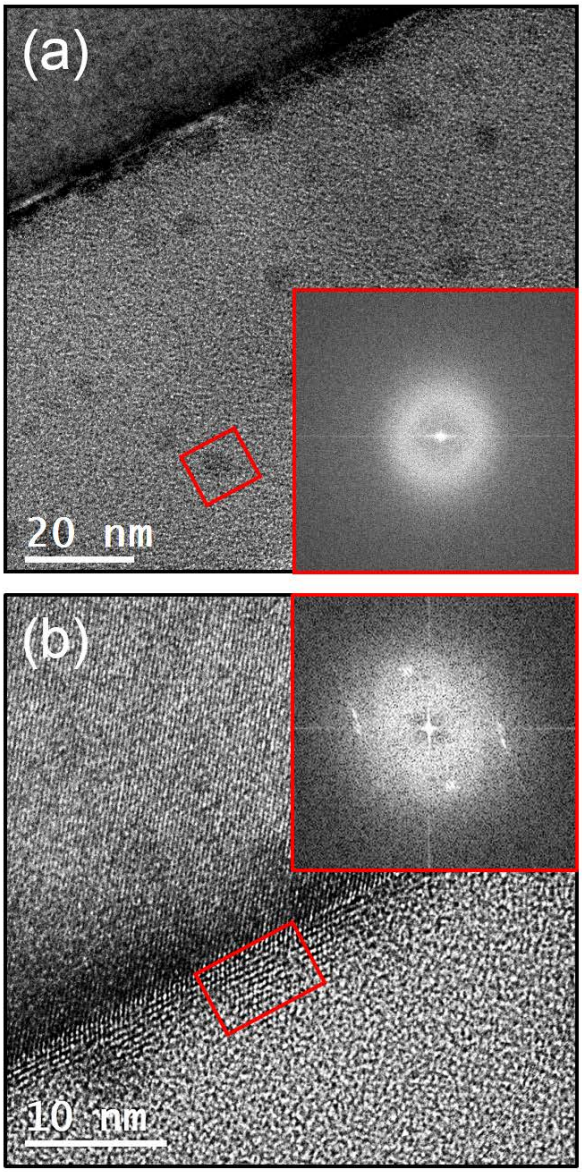

Figure 5: (a) TEM image of a Ce^{3+}-doped SiO_xN_y thin film (42 at. % of N) annealed at 1180 °C displaying homogeneously distributed amorphous RE clusters. (b) HRTEM image of the same sample centered at the interface with the Si substrate. Dark clusters with ordered lattice fringes are observed. Insets show the Fast Fourier Transform performed over such clusters in a localized region marked with a red box, confirming the presence of crystalline planes with an inter-atomic distance that varies from sample to sample from 0.2 nm to 0.4 nm.

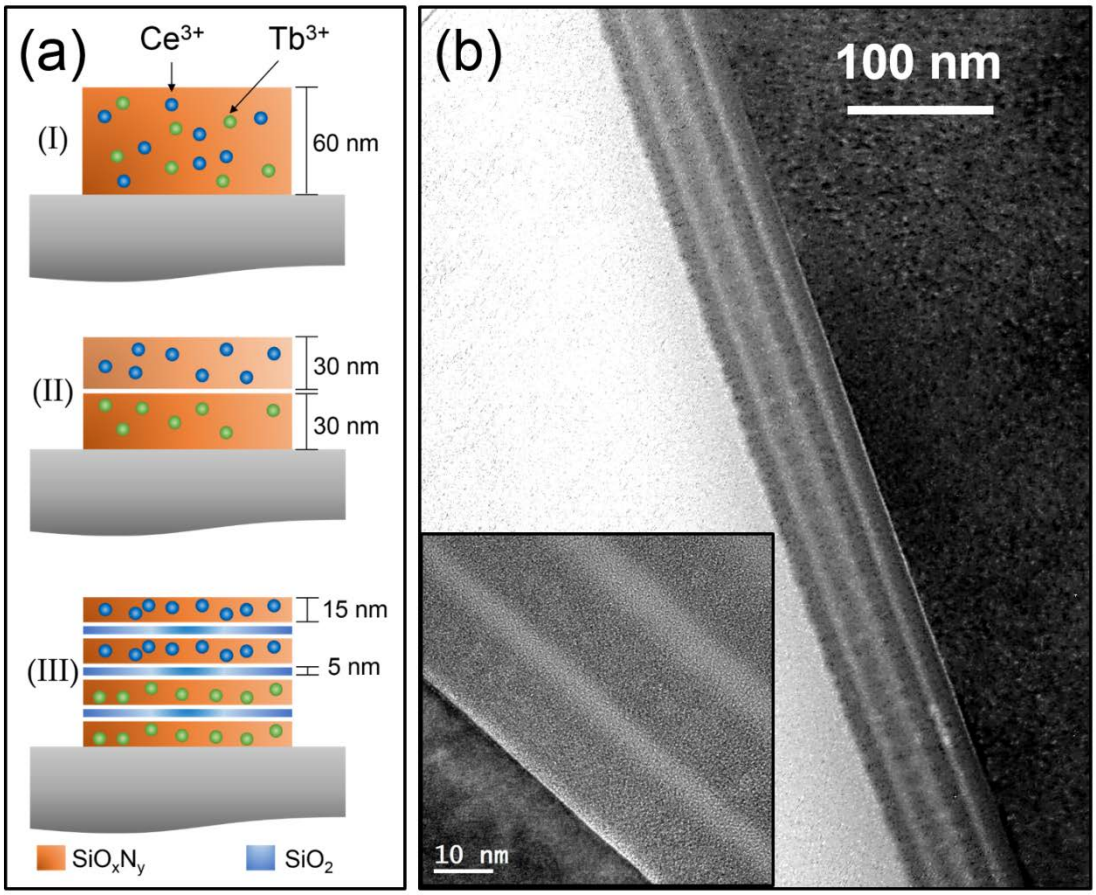

Figure 6: (a) Sample description, being (I) a Ce^{3+} and Tb^{3+} co-doped SiO_xN_y thin film 60 nm thick with 42 at. % of N; (II) a bilayer composed by a Ce^{3+}-doped SiO_xN_y single layer and a Tb^{3+}-doped SiO_xN_y single layer, each one 30 nm thick; and (III) a multilayer made of 2 layers of Tb^{3+}-doped SiO_xN_y and 2 layers of Ce^{3+}-doped SiO_xN_y (each sub-layer with a thickness of 15 nm), separated by SiO_2 spacers of 5 nm. All SiO_xN_y layers have a nitrogen content of 42 at. %. (b) HRTEM image of the multilayer design (structure (III), as-deposited sample). The inset shows a magnified region of the multilayer close to the Si substrate, for a sample annealed at 1180 C for 1 h.

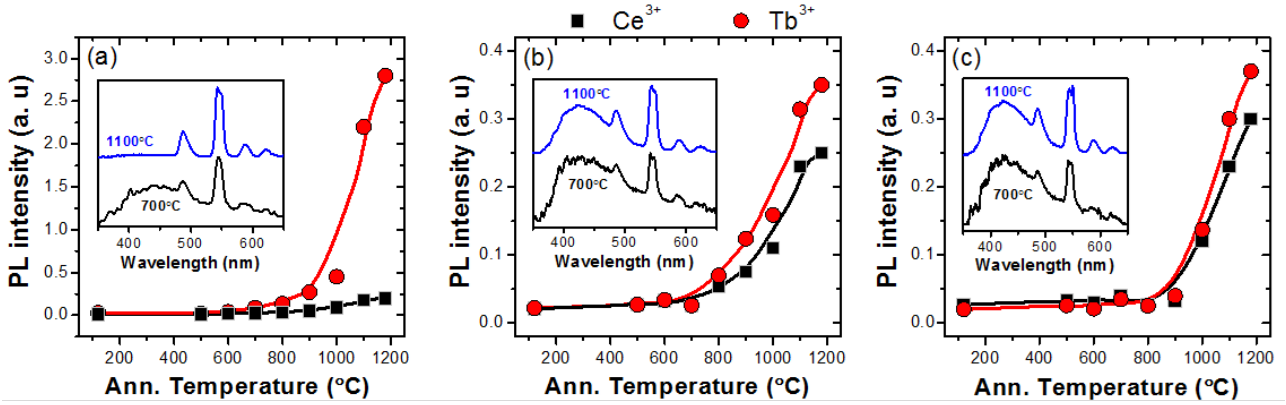

Figure 7: PL characterization of Ce^{3+} and Tb^{3+} co-doped SiO_xN_y thin films, standing for: (a) the single layer, (b) the bilayer and (c) the multilayer. Red and black lines display the evolution of the PL intensity of the Tb^{3+} and Ce^{3+} most intense radiative transitions, respectively. The y-axis scales are comparable. The inset illustrates the normalized PL spectra of different samples after undergoing an annealing treatment at 700 °C (bottom spectra) or at 1100 °C (upper spectra, arbitrarily up-shifted) for 1h.

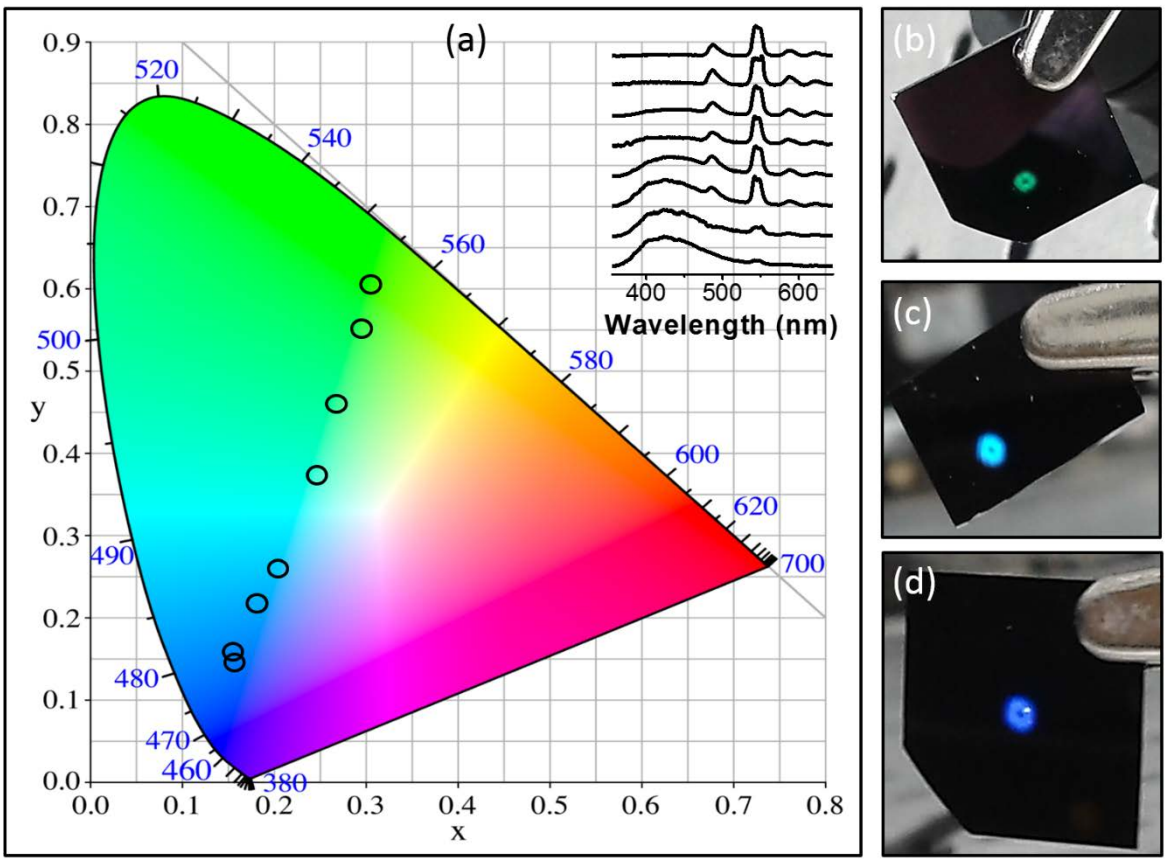

Figure 8: a) XYZ coordinates of 8 different Ce^{3+}- and/or Tb^{3+}-doped thin films in the 1931 CIE chromaticity diagram. The PL spectrum of each sample is displayed at the inset, from the cobalt blue emission (at the bottom) up to the emerald green (most up-shifted spectrum). A representative example of the emission of thin films is displayed in (b), (c) and (d). Pictures were taken with a smart phone camera of 5 Mega Pixels.

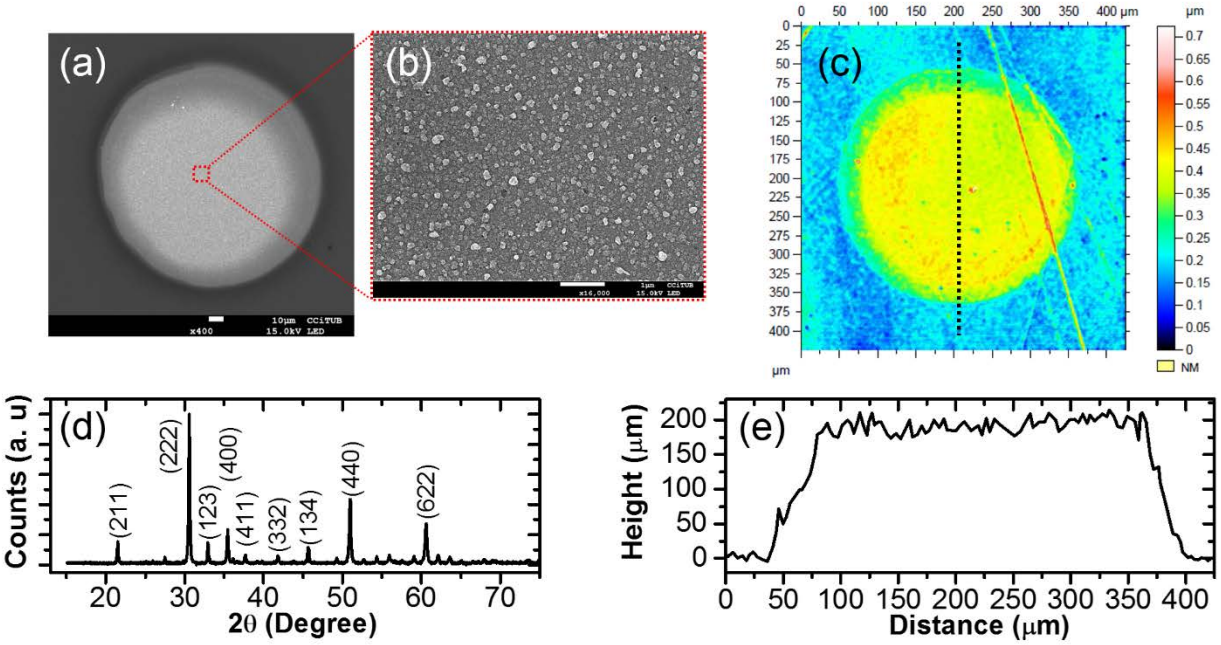

Figure 9: (a) SEM top view image of a single ITO electrode. (b) zoom-in image of a specific position at the ITO electrode, showing a granular morphology. (c) Top view image of a single ITO electrode, taken by using optical interferometry. The scratches observed at the right part of the electrode belong to the acquisition system (partial damaging of the mirror) and not to the sample. (d) XRD measurement of ITO, with several diffraction peaks belonging to different crystallographic planes. (e) Interferometry profile of the ITO electrode, taken along the dotted line shown in (c).

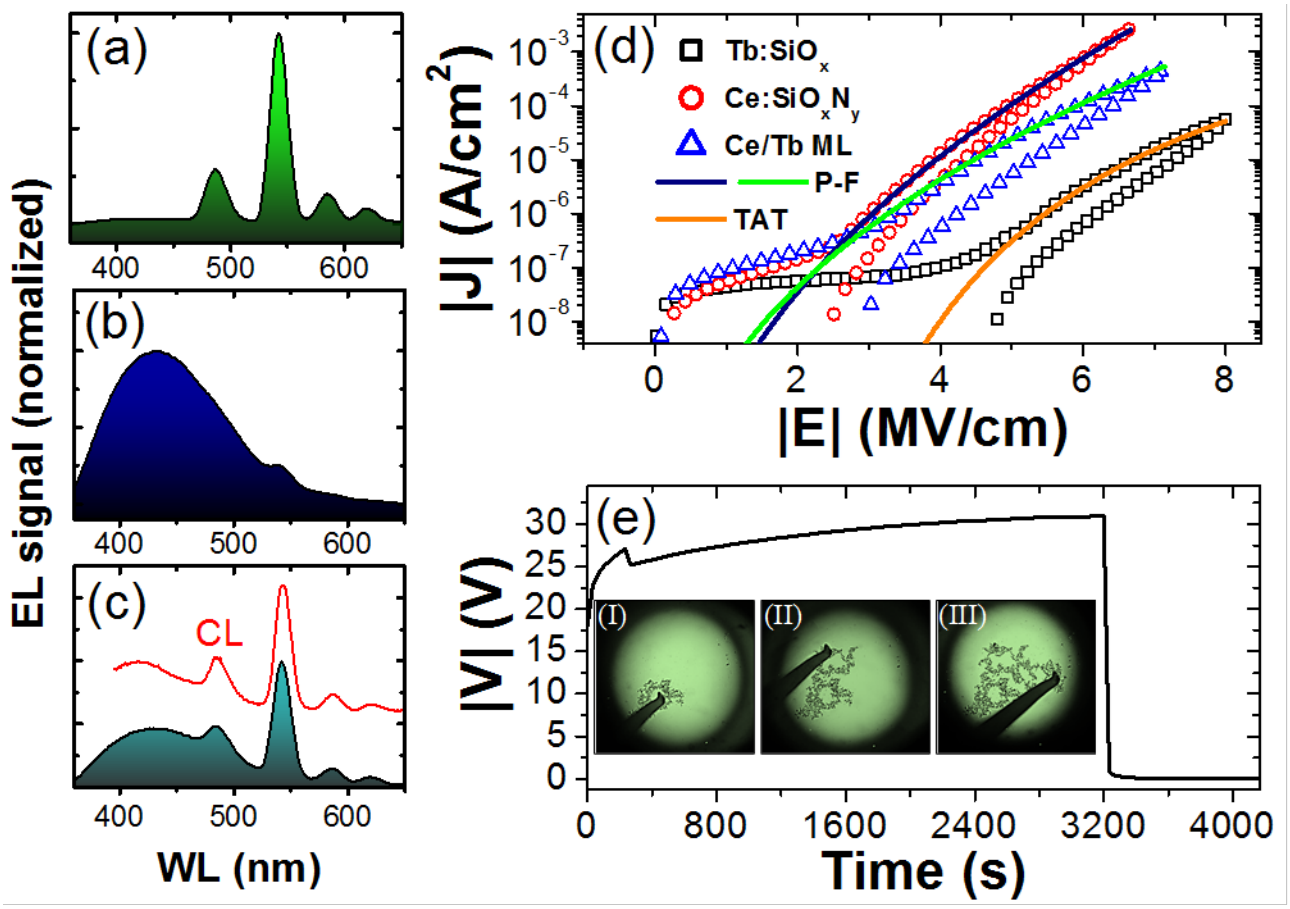

Figure 10: (a), (b) and (c) show the normalized EL spectra of electroluminescent test devices under a constant current density of $3 \cdot 10^{-5}$ A/cm^2 (panel (a), Tb:SiO$_x$), 10^{-3} A/cm^2 (panel (b), Ce:SiO$_x$N$_y$) and $3 \cdot 10^{-4}$ A/cm^2 (panel (c), Ce/Tb ML). Panel (c) also shows the measured CL spectrum of the sample for comparison (arbitrarily up-shifted). (d) J-E characteristic, in absolute values, of the electroluminescent test devices containing either a luminescent Tb^{3+}-doped SiO_2 layer (empty squares), a Ce-doped SiO_xN_y single layer with 42 at. % of N (empty dots) or a Ce^{3+} and Tb^{3+} co-doped multilayer as in the approach III of figure 6 (empty triangles). (e) V-t characteristic, in absolute values, of the Ce:SiO$_x$N$_y$ device under a constant current density of 10^{-3} A/cm^2. The inset shows a chronological sequence of top views of the device for different polarization points. The green circular region and the black shadow correspond to the ITO electrode and the polarization tip, respectively. The green color corresponds to the combined effect of the absorbed and backscattered wavelengths of the microscope backlight.

Table I: Deposition parameters, film thickness and composition of studied samples. Each sample has been annealed under 8 different temperatures: 500, 600, 700, 800, 900, 1000, 1100, and 1180 °C. Estimated experimental errors for the atomic concentration are; ~ 5×10^{19} at./cm^3 for Ce and Tb elements, ~ 5×10^{20} at./cm^3 for N and O and ~ 1×10^{20} at./cm^3 for Si.

Film	**SiH_4/Ar (sccm)**	**N_2/Ar (sccm)**	**O_2/Ar (sccm)**	**Si (at./cm^3)**	**N (at./cm^3)**	**O (at./cm^3)**	**Thickness (nm)**
Ce^{3+} or Tb^{3+}-doped thin films (single layer)							
#1	2.5	0	25	2.1×10^{22}	--	5×10^{22}	100
#2	2.5	5	20	2.1×10^{22}	5×10^{20}	4.9×10^{22}	97
#3	2.5	10	15	2.2×10^{22}	2.5×10^{21}	4.5×10^{22}	92
#4	2.5	15	10	2.2×10^{22}	9×10^{21}	4×10^{22}	94
#5	2.5	20	5	2.2×10^{22}	1.9×10^{22}	2.8×10^{22}	88
#6	2.5	25	0	2.3×10^{22}	2.8×10^{22}	1.5×10^{22}	80
Ce (Tb) doping concentration: ~ 4×10^{20} at./cm^3							
$Ce^{3+}$and Tb^{3+}co-doped thin film (single layer)							
Ce:Tb:SiO_xN_y	2.5	25	0	2.2×10^{22}	2.9×10^{22}	1.3×10^{22}	63
Ce doping concentration: ~ 2×10^{20} at./cm^3 Tb doping concentration: ~2.3×10^{20} at./cm^3							
$Ce^{3+}$and Tb^{3+}co-doped bilayer							
Ce:SiO_xN_y	2.5	25	0	2.2×10^{22}	2.7×10^{22}	1.2×10^{22}	28
Tb:SiO_xN_y	2.5	25	0	2.3×10^{22}	2.6×10^{22}	1.4×10^{22}	31
Ce doping concentration: ~ 1.7×10^{20} at./cm^3 Tb doping concentration: ~2.5×10^{20} at./cm^3							
$Ce^{3+}$and Tb^{3+}co-doped multilayer *(Ce ~ 1.3×10^{20} at./cm^3 / Tb ~ 1.8×10^{20} at./cm^3)*							
Tb:SiO_xN_y	2.5	25	0	2.2×10^{22}	2.4×10^{22}	1.6×10^{22}	13
SiO_x	2.5	0	25	2×10^{22}	--	4.7×10^{22}	7
Tb:SiO_xN_y	2.5	25	0	2.1×10^{22}	2.3×10^{22}	1.4×10^{22}	14
SiO_x	2.5	0	25	2.2×10^{22}	--	5.1×10^{22}	5
Ce:SiO_xN_y	2.5	25	0	2.2×10^{22}	2.6×10^{22}	1.4×10^{22}	16
SiO_x	2.5	0	25	2.3×10^{22}	--	5×10^{22}	6
Ce:SiO_xN_y	2.5	25	0	2.2×10^{22}	2.6×10^{22}	1.5×10^{22}	15
Ce doping concentration: ~ 1.6×10^{20} at./cm^3 Tb doping concentration: ~2.2×10^{20} at./cm^3							